

Three-dimensional neutron far-field tomography of a bulk skyrmion lattice

Received: 30 August 2022

Accepted: 13 July 2023

Published online: 14 August 2023

 Check for updates

M. E. Henderson ^{1,2,9}✉, B. Heacock ^{3,9}, M. Bleuel ³, D. G. Cory^{1,4},
C. Heikes ³, M. G. Huber³, J. Krzywon ³, O. Nahman-Levesque^{1,2},
G. M. Luke ^{5,6}, M. Pula⁵, D. Sarenac ^{1,7}, K. Zhernenkov^{1,8} & D. A. Pushin ^{1,2}✉

Magnetic skyrmions are localized non-collinear spin textures, characterized by an integer topological charge. Commonly observed in thin systems as two-dimensional sheets, in three dimensions skyrmions form tubes that are thought to nucleate and annihilate along their depth on points of vanishing magnetization. However, a lack of techniques that can probe the bulk of the material has made it difficult to perform experimental visualizations of skyrmion lattices and their stabilization through defects. Here we present three-dimensional visualizations of a bulk $\text{Co}_8\text{Zn}_8\text{Mn}_4$ skyrmion lattice through a tomographic algorithm applied to multiprojection small-angle neutron scattering measurements. Reconstructions of the sample show a disordered skyrmion lattice exhibiting three-dimensional topological transitions through emergent (anti)monopole branching and segmentation defect pathways. Our technique provides insights into skyrmion stabilization and topological transition pathways in a bulk skyrmion lattice, guiding the future development and manipulation of skyrmion materials for spintronic applications.

Magnetic skyrmions manifest as spin vortices, whose topological protection drives particle-like properties and condensation into thermodynamically stable phases in an external magnetic field^{1–4}. Most commonly observed as two-dimensional (2D) structures in metallic materials^{5–10}, their quantized emergent magnetic flux^{1,11–13}, which characterizes the Berry phase an electron accrues when following the local magnetization adiabatically¹⁴, generates unique transport phenomena^{15–17}, multiferroic behaviour¹⁸ and electric controllability via ultralow current densities^{12,19}. Such a culmination of features sees skyrmions as promising candidates for next-generation low-power spintronic information-processing and storage devices^{20–22}.

In three dimensions, the uniform stacking of the 2D skyrmion spin structure produces skyrmion tubes elongated along the external magnetic field direction, thought to penetrate surface to surface^{23,24}.

In physical bulk crystal systems at non-zero temperature, a finite density of defects exists, interrupting the skyrmion string propagation²⁵. Because the emergent flux that defines skyrmions is quantized, their nucleation and termination is mediated by emergent magnetic charges that must also be quantized¹³. Skyrmion tube segmentation and branching via emergent magnetic monopoles and antimonopoles (denoted S^+ , S^- , B^+ and B^- , respectively) are believed to mediate skyrmion topological transitions²⁶. Motion of such defects in response to changes in external parameters, such as field or temperature conditions, have been proposed to drive a change in skyrmion topology through the unwinding of individual skyrmions^{25,26} and the zipping and unzipping of neighbouring skyrmion tubes^{13,26,27}. Since total emergent charge is conserved, skyrmionic transitions can only take place in three dimensions when emergent (anti)monopoles are either pinned to a material

¹Institute for Quantum Computing, University of Waterloo, Waterloo, Ontario, Canada. ²Department of Physics & Astronomy, University of Waterloo, Waterloo, Ontario, Canada. ³National Institute of Standards and Technology, Gaithersburg, MD, USA. ⁴Department of Chemistry, University of Waterloo, Waterloo, Ontario, Canada. ⁵Department of Physics and Astronomy, McMaster University, Hamilton, Ontario, Canada. ⁶Brockhouse Institute for Materials Research, Hamilton, Ontario, Canada. ⁷Department of Physics, University at Buffalo, State University of New York, Buffalo, NY, USA. ⁸Jülich Centre for Neutron Science at Heinz Maier-Leibnitz Zentrum, Forschungszentrum Jülich GmbH, Garching, Germany. ⁹These authors contributed equally: M. E. Henderson, B. Heacock. ✉e-mail: mehenderson@uwaterloo.ca; dmitry.pushin@uwaterloo.ca

defect or jammed in place and unable to overcome the activation energy required to travel to the material surface or reach an oppositely charged monopole to annihilate^{5,27,28}.

Examinations of skyrmions using 2D imaging have revealed a myriad of in-plane skyrmion string deformations including elongated structures¹³ and bent skyrmion strings that terminate on the surface²⁹ or form at edges²⁸, while three-dimensional (3D) imaging in confined systems has revealed axial modulation of skyrmion tubes³⁰. In all of these instances, the physical systems being probed are subject to constricted geometries by virtue of the thin plate or needle-shaped samples required by the techniques. This introduces confinement effects, causing the system to exhibit drastically different energetics to those of bulk samples, favouring surface pinning³¹ and edge interactions^{28,32,33}, which affect skyrmion formation, shape, interactions, dynamics and stabilization. Recent advances in the imaging and reconstruction of 3D magnetization vector fields have been made using X-ray magnetic microscopy^{34,35} and nanotomography^{36,37} techniques, exploiting dichroism in magnetic scattering and element-specific absorption contrast. However, such methods maintain low penetration depths, bounded material thicknesses and compositions and require vacuum-compatible setups that typically limit angular sampling³⁷. A recent study³⁸ confirmed the presence of interrupted and merging-type skyrmion strings in a sparsely populated micrometre-sized thin plate needle-shaped sample of $\text{Mn}_{1.4}\text{Pt}_{0.9}\text{Pd}_{0.4}\text{Sn}$ using scalar magnetic X-ray tomography. The observations, however, are limited to individual skyrmion strings in a sample thickness only a few times the skyrmion tube diameters, whose confined geometry and thickness gradient fundamentally alters the skyrmions shape and behaviour; bulk lattice skyrmion behaviour has yet to be experimentally observed.

Small-angle neutron scattering (SANS) is sensitive to bulk scattering features, enabling studies of truly bulk skyrmionic systems along different paths through the sample's phase diagram. In particular, spatially averaged depth information may be obtained by forming rocking curves, integrating over one or more diffraction peaks as a function of sample angle, to extract the longitudinal correlation length of a skyrmion lattice⁴. The effects of recent external magnetic field and temperature history on jammed states has been shown using SANS, where skyrmion lattice defect densities were reduced using an ordering sequence where the external magnetic field is rocked relative to the sample³⁹. Rocking the sample in the field^{39,40} produces skyrmion lattice reorientations that disentangle the jammed state, promoting additional skyrmion formation^{39,40}, unless the segmentation defect creation barrier is too high or the pinning potential is too strong to liberate existing defects^{14,40,41}.

Whereas previous studies are confined to surface-level techniques, confined systems or integral far-field SANS measurements that cannot produce real-space representations of the sample, here we perform tomography of the thermal equilibrium triangular skyrmion lattice phase to generate a 3D mean scattering feature reconstruction (MSFR) of a bulk skyrmion lattice. While existing neutron scattering tomography techniques have applied phase-retrieval algorithms to multiprojection ultra-SANS datasets to reconstruct 2D scattering length density maps of periodic structures⁴², the technique presented here takes somewhat of a divergent approach, coupling the angular projection datasets with a free-energy regularization. In particular, our reconstruction algorithm consists of first forming an estimator of a multiprojection set of SANS measurements by operating on the incoming neutron state with a forward operator, which takes the MSFR volume as its main input. Next, the sum of weighted residuals between the estimated and measured SANS patterns for multiple projections is minimized with respect to the MSFR. Without integrating over peak areas before forming the rocking curve, the weighted sum of measurement residuals χ^2 is sensitive to shifting peak locations, shapes, intensities and correlations. The number of free parameters depends on the chosen MSFR volume but will usually be larger than the number of data

points in the set of SANS images. The large degeneracy of possible solutions and the danger of overfitting the data is overcome by adding a free-energy regularizing functional to the objective function $f = \chi^2 + \beta\mathcal{F}$, where \mathcal{F} is the free energy of the MSFR and β is a Lagrange multiplier reminiscent of a Boltzmann factor. The free energy includes the Heisenberg exchange, Dzyaloshinskii–Moriya exchange and external field Zeeman terms and could be made to include additional interactions that are functionals of the spin density, although such terms are beyond the scope of the present work. Knowledge of the functional form of the free energy and average magnetization of the phase is therefore required for the application of this technique to a magnetic system. Similar techniques are often used in traditional computed tomography algorithms, in which case the total variation can be used as a regularizing functional⁴³. The resulting MSFRs may be interpreted as containing the types of structures, and their densities, which are common within the sample. However, there is no portion of the sample that looks exactly like a MSFR, and there are a large number of possible MSFRs that would converge on a minimum of the objective function. Moreover, since the reconstructed magnetization volumes are representative of the bulk, they will not produce surface specific features (such as surface twisting^{24,44}) unless it is frequent throughout the sample, comprising a sizable volume fraction of the magnetic features. One can also view minimizing the objective function as performing a micromagnetic simulation with the χ^2 providing the local interaction and pinning potential terms in the free energy that cause lattice defects, thereby enforcing the lattice correlation lengths and structure encoded in the SANS patterns.

Multiprojection SANS measurements were made (Fig. 1) using an above room temperature skyrmion host $\text{Co}_8\text{Zn}_8\text{Mn}_4$ previously characterized in ref. 40. This class of materials has been studied across a variety of techniques including SANS^{3,40,41,45–47}, magnetic susceptibility^{3,40,45,46} and Lorentz transmission electron microscopy^{3,45}. Given the disordered nature of the thermal equilibrium triangular lattice skyrmion phase as explored in refs. 40,41, a skyrmion ordering sequence in which the sample was rotated in the magnetic field was first applied to precipitate ordered and oriented skyrmion lattices (Methods). Collection of the tomographic angular projections was then achieved by rotating the sample and magnetic field coincident about the vertical axis specified in Fig. 1. The determination of the range and number of projections that should be collected for a given magnetization volume, or sample, is set by the correlation lengths of the phase. In the ideal case, the angular range should be sufficiently large so as to capture the entire decay of the rocking curve. Rotations past this point do not enhance the data unless there exist large off-axis domain structures or spin geometries in which the propagation wavevector lies parallel to the incident neutron direction. For example, conical domains may be probed by collecting angular projections about the perpendicular sample-field geometry; however, these are left as the subject of our future experimental explorations. For the case of highly disordered states characterized by long rocking curves with persistent non-zero angular intensities, this can lead to large angular ranges for the tomographic datasets, and can also present challenges for the rotation of cumbersome cryomagnets in the limited sample space available on typical SANS beamlines. In the experiment presented here, the ordered skyrmion sample and magnetic field were rotated through 30 projections over a 5.8° angular range, limited by the geometry of the guide field coils (Fig. 2a). Application of the ordering sequence seeks to both enhance the longitudinal and transverse correlation lengths of the phase while precipitating an oriented monodomain skyrmion lattice. Therefore, the ordering sequence should refocus intensity to the central peak of the rocking curve, while minimizing its full width at half-maximum and any potential persistent non-zero angular intensity offsets arising from misoriented chiral domains. As a result, the initial application of the ordering sequence enforces our measured angular range, while some of the rocking curve extrapolation performed at

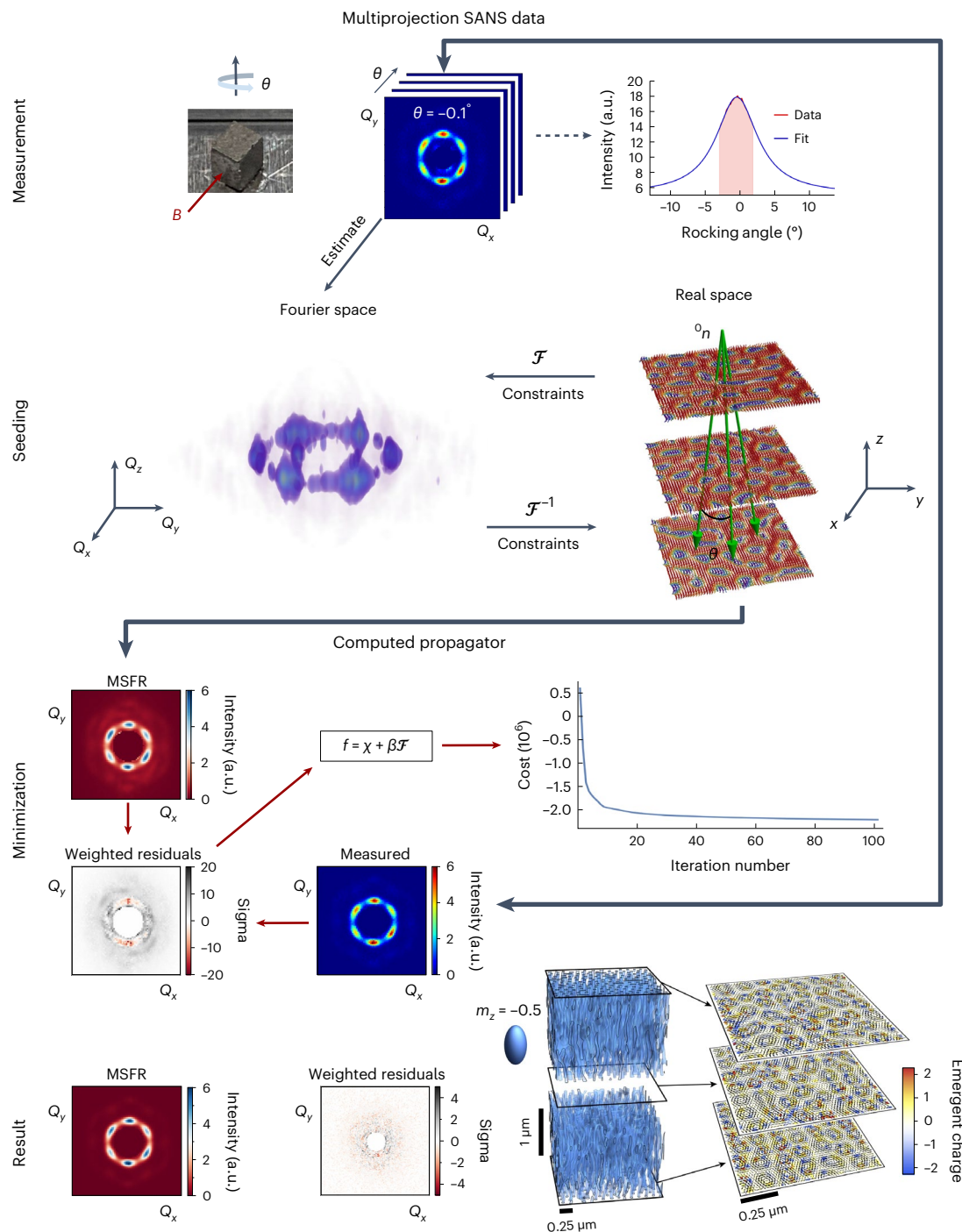


Fig. 1 | Reconstruction technique applied to a bulk skyrmion material.

Schematic outlining the reconstruction technique, beginning with the collection of experimental SANS angular projections (top) and ending with the output MSFR (bottom). The experimental sample-field geometry used during tomographic rotations is shown, where the sample and magnetic field were rotated coincident about an angle θ ensuring a fixed magnetic orientation parallel to the surface normal of the sample. The rocking curve is plotted for one of the horizontal peaks, showing the measured and extrapolated

regions of the Lorentzian curve. Estimated and measured SANS patterns are shown for the initial and final MSFR, including their weighted residuals and minimization of the cost function. The reconstruction is shown for the entire $12.3 \mu\text{m}^3$ ($1.8 \mu\text{m} \times 1.8 \mu\text{m} \times 3.7 \mu\text{m}$) MSFR volume, with blue contours outlining the skyrmion tubes for an out-of-plane magnetization, $m_z = -0.5$. Enlarged 2D skyrmion spin textures are shown for three depths along the reconstruction with highlighted emergent magnetic charges. a.u., arbitrary units.

lower wave vectors, Q , gets filled in by the average magnetization parameter, $\langle m_z \rangle$, and free-energy term. To determine the implications for how a limited-projection dataset would affect our results, we reconstructed digital phantoms under both ideal conditions, where SANS data were simulated for 31 projections between $\pm 15^\circ$ about both axes

(no compound rotations) and the actual experimental projections (see Methods and the ideal versus limited-projection datasets in the Supplementary Information).

2D slices of the measured and reconstructed SANS images, weighted residuals and MSFRs are shown for the bulk sample and

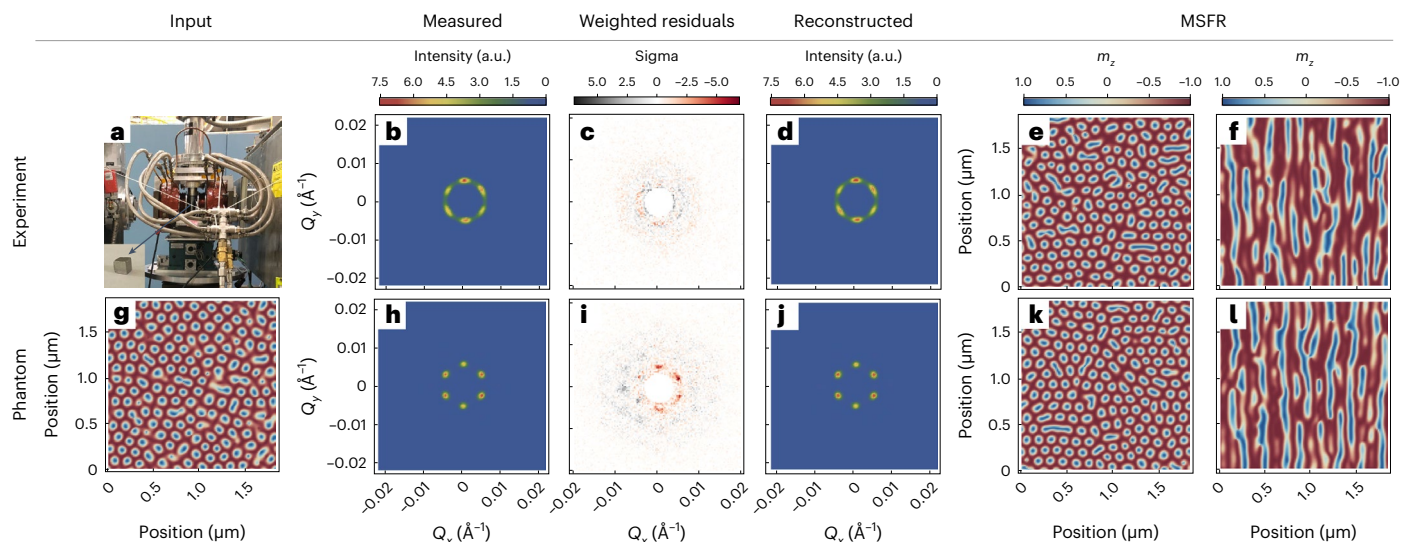


Fig. 2 | Magnetization slices of reconstructed experimental and phantom datasets. **a–f**, Experimental setup (**a**), measured SANS image (**b**) reproduced from ref. 40, minimized weighted residuals (**c**), reconstructed SANS image (**d**), and xy (**e**) and xz (**f**) slices of the MSFR. **g–i**, The corresponding plots for the phantom B limited-projection dataset (see highlighted row in Table 1) where **g** is the simulated input magnetization, **h** is the simulation SANS pattern and

i–l are the same as in **c–f**, respectively. All SANS images are shown for the zero projection, with the guide field and sample aligned parallel to the neutron beam. The xy and xz magnetization slices are shown for a $1.8 \mu\text{m} \times 1.8 \mu\text{m}$ area of the MSFR, showing the full in-plane magnetization slice and half of the longitudinal magnetization slice.

phantom set B with average magnetizations of 0.42 and 0.41 (Fig. 2), respectively. Videos showing magnetization and topological defects as a function of depth for the sample MSFR, phantom B and its corresponding limited-projection and ideal MSFRs are available as Supplementary Videos 1–4. The full set of videos for every dataset listed in Table 1 is available at the online repository found in ref. 48. Since the reconstruction technique does not provide a one-to-one spatial mapping to any volume within the sample, deviations between Fig. 2g,k are expected. However, comparison between the two in-plane slices shows the presence of similar topological structures, transitions and skyrmion packing densities. A more accurate and comprehensive comparison entails looking at the entire input and MSFR volumes for average features and their densities. Average magnetization, topological saturation and defect densities are compared in Table 1. Phantoms were generated with the external field near the helical-skyrmion boundary (phantom A), the ideal value (phantom B) and the ferromagnetic-skyrmion boundary (phantom C). The choice of Zeeman term h was set such that the average magnetization of the reconstructions matched those estimated through magnetic susceptibility measurements. The required weighting of the Zeeman term h to achieve the average magnetization that was estimated from d.c. susceptibility was affected by the value of χ^2 . The favoured MSFRs are thus those with values of h that produce the estimated average magnetization and they are highlighted in Table 1. The agreement between phantom and MSFR is reasonable for phantoms B and C, with deviations between ideal and limited-projection datasets probably arising owing to the truncated rocking curve of the limited datasets. However, the MSFR for phantom A overestimates the branching defect density. This is probably attributable to the seeding, where phantom A transitioned from an average magnetization of $\langle m_z \rangle = 0.4$ to $\langle m_z \rangle = 0.33$ during the free-energy relaxation (Methods), while the MSFR had a net magnetization change of $\langle m_z \rangle = 0.35$ to $\langle m_z \rangle = 0.32$, suggesting hysteresis-like effects can impact the fidelity of the reconstructions. Such effects are reminiscent of real samples, wherein sample histories and trajectories through phase space may alter the stability, chiral and topological volume fractions and defect densities of the phase^{49–51}. Future studies may incorporate variations

of the estimated $\langle m_z \rangle$ parameter to simulate and incorporate these hysteresis effects.

The sample MSFR topological saturation $N_{\text{sk}}/N_{\text{max}}$ is found to be 63% of that of a perfect skyrmion triangular lattice with the same reciprocal space scattering location, Q_0 . This is reflected by the presence of transverse and longitudinal lattice distortions. In particular, skyrmion voids, bimerons and elongated spin structures present in the 2D MSFR magnetization slices reduce the number of skyrmions from that of an ideal hexagonally packed lattice. Similarly, interruption of the skyrmion strings along their length may be visualized by taking an $x-z$ slice of the MSFR as shown in Fig. 2f.

3D visualizations of portions of the sample MSFR show skyrmion nucleation and annihilation along their depth, where segmentation S^\pm and branching B^\pm (anti)monopoles mediate the change in topology at skyrmion transition points (Fig. 3e). These features are similar to those observed for simulations of skyrmion annihilation in three dimensions through helical and conical pathways^{13,26,27}. Notably, some branching events are observed to occur along wave vectors Q that are offset by 60° from the horizontal nearest-neighbouring skyrmion, producing a skyrmion twisting effect (Fig. 3a). Conversely, some instances of segmentation events exhibit pairs of S^\pm (anti)monopoles that cup skyrmions, producing spatially localized skyrmion filaments that extend longitudinally over a few lattice periods (Fig. 3d) and are reminiscent of magnetic torons⁵². Given the field history of the sample, wherein saturation to the ferromagnetic phase was performed before collection of the tomography data, these structures may represent a skyrmion survival mechanism in the field-polarized state via magnetic torons on defect pinning sites⁴¹. Future studies will be performed to examine the prevalence of these structures as a function of field history and average magnetization, providing insight into skyrmion elongation and stabilization mechanisms.

The energy source required for emergent (anti)monopole creation may derive from internal chemical disorder present in the material (such as in material imperfections or site disorder^{9,14,26}), thermal activation^{53–55} and the external magnetic field setting relative to the helical and ferromagnetic phase boundaries^{13,29,54}. For the case of the magnetic field setting, segmentation and branching (anti)monopoles

Table 1 | Zeeman term weight in reduced field units h , seeded average magnetization $\langle m_z \rangle_{\text{seed}}$, final average magnetization $\langle m_z \rangle$, topological saturation $N_{\text{sk}}/N_{\text{max}}$ and defect densities ρ of the phantoms and associated MSFRs and sample MSFR

	h	$\langle m_z \rangle_{\text{seed}}$	$\langle m_z \rangle$	$N_{\text{sk}}/N_{\text{max}}$ (%)	$\rho_{\text{branch}} (\mu\text{m}^{-3})$	$\rho_{\text{seg}} (\mu\text{m}^{-3})$	$\rho_{\text{tot}} (\mu\text{m}^{-3})$
Phantom A	0.56	0.40	0.33	65	101	37	138
MSFR A, ideal	0.50	0.30	0.28	52	322	7	329
	0.60	0.35	0.32	59	238	13	251
	0.75	0.40	0.37	65	150	26	176
MSFR A, lim. proj.	0.50	0.30	0.30	56	299	9	308
	0.60	0.35	0.34	60	233	13	246
Phantom B	0.75	0.40	0.41	68	47	40	87
	0.60	0.35	0.35	62	138	10	148
	0.75	0.40	0.38	64	115	12	127
MSFR B, ideal	0.87	0.45	0.42	72	53	31	84
	0.60	0.35	0.35	60	166	6	172
	0.75	0.40	0.41	67	88	16	104
MSFR B, lim. proj.	0.87	0.45	0.45	69	53	31	84
	0.94	0.40	0.47	73	13	103	115
Phantom C	0.80	0.42	0.41	69	133	27	161
	0.94	0.47	0.46	72	54	56	110
	1.08	0.52	0.49	72	21	91	112
MSFR C, ideal	0.80	0.42	0.43	69	126	26	152
	0.94	0.47	0.49	72	46	63	109
	1.08	0.52	0.54	71	23	95	119
MSFR C, lim. proj.	0.50	0.30	0.25	53	214	6	220
	0.60	0.35	0.35	59	163	13	176
	0.75	0.40	0.42	63	118	21	139
	0.87	0.45	0.48	66	69	37	106

The highlighted rows correspond to the reconstructions that most closely match the known $\langle m_z \rangle$ parameters—calculated from input phantoms or extracted through susceptibility measurements. The reduced field is fixed; all other parameters are computed from the spin density. lim. proj., limited projection.

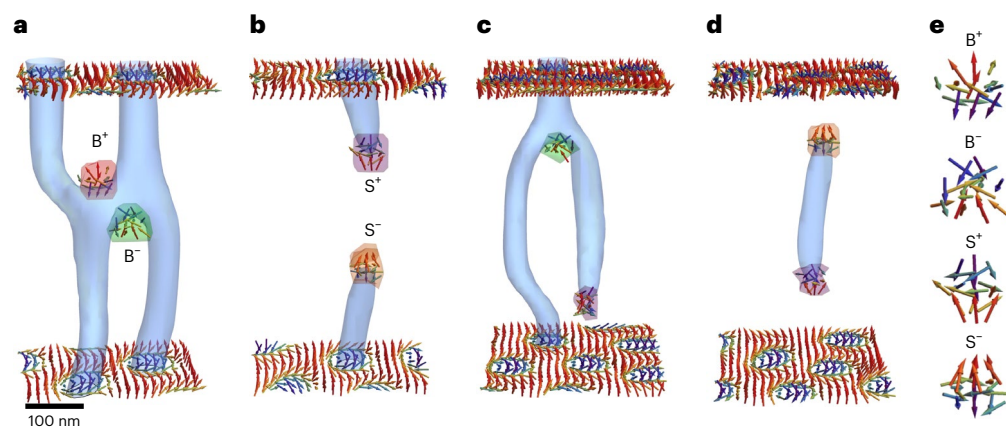


Fig. 3 | 3D Skyrmion tubes and their topological transition defect pathways. Characteristic topological transitions present in the MSFR showing branching (B) and segmentation (S) (anti)monopole pathways. Skyrmion topological transitions accompanied by a branching monopole-antimonopole pair (a), segmentation monopole-antimonopole pair (b), combination of segmentation monopole and branching antimonopole (c), and a localized skyrmion filament structure cupped by a segmentation monopole-antimonopole pair (d). The blue contours outline the skyrmion tubes where the out-of-plane magnetization $m_z = -0.5$. Some of the skyrmion tubes are masked to highlight the regions

undergoing changes in topology. Emergent magnetic charge density contours are shown for the two types of skyrmion topological transition processes with S^+ , S^- , B^+ and B^- corresponding to purple, orange, red and green, respectively. Branching and segmentation emergent (anti)monopoles are observed to occur at transition points along the tubes, displaying distinct spin textures determined by the sign of $\partial_z m_z$. e, Enlarged spin textures are shown for the labelled branching and segmentation (anti)monopoles with each spin corresponding to one voxel. All skyrmion features are shown for a depth of 37 voxels, equating to 531 nm (Methods).

are thought to control skyrmion annihilation upon increasing and decreasing fields, respectively^{13,27,56}. This is reinforced by reconstructions performed on equivalent datasets under different average magnetization and reduced field h conditions; a shifting prevalence from branching defects in the low-field case to segmenting defects in the high-field case is observed.

The preferred sample MSFR shows segmentation and branching (anti)monopoles seemingly jammed in place and unable to travel to the sample surfaces or annihilate. The observed defect densities could be due to pinning potentials in the material that would trap the (anti)monopoles and inhibit their motion¹⁴. In this case, the prevalence of these structures may indicate the degree of internal chemical disorder, providing snapshots of magnetic defect pinning centres. Alternatively, these features may be evidence of an incomplete ordering sequence, wherein the limited magnetic field directions during rotation did not allow the monopoles to propagate along enough angular paths in the sample to completely break up the jammed labyrinth domains³⁹. Future SANS tomography measurements taken as a function of skyrmion ordering could decouple these two possibilities. Implementation with structured neutron beams, which possess an analogous non-trivial winding character in spin⁵⁷ or phase^{58,59}, may provide estimates of the magnetic defect densities based on the vertical widening of the skyrmion peaks in the transverse geometry. Alternatively, the defects themselves may be viewed as the magnetic equivalent of phase singularities, capable of generating topological neutron states for probing nanometric sample topologies.

We have shown experimental visualizations of the 3D character of a bulk skyrmion lattice through MSFR, generated via a SANS tomography technique. The present results uncover the stabilization and evolution of a triangular skyrmion lattice in the bulk through 3D topological transitions that exhibit a mixture of distinctive segmenting and branching (anti)monopole defects. Exotic features for these two event types are observed in the MSFR, characterized by skyrmion twisting during branching events and localized skyrmion filament structures cupped by S^\pm (anti)monopoles. Our SANS tomography techniques provide unique insights into skyrmion formation, annihilation and transition processes through (anti)monopole defects, opening the door to future studies of bulk micromagnetic materials on unprecedented length scales, including skyrmion and emergent (anti)monopole structure, behaviour and dynamic processes.

Online content

Any methods, additional references, Nature Portfolio reporting summaries, source data, extended data, supplementary information, acknowledgements, peer review information; details of author contributions and competing interests; and statements of data and code availability are available at <https://doi.org/10.1038/s41567-023-02175-4>.

References

- Nagaosa, N. & Tokura, Y. Topological properties and dynamics of magnetic skyrmions. *Nat. Nanotechnol.* **8**, 899–911 (2013).
- Mühlbauer, S. et al. Skyrmion lattice in a chiral magnet. *Science* **323**, 915–919 (2009).
- Tokunaga, Y. et al. A new class of chiral materials hosting magnetic skyrmions beyond room temperature. *Nat. Commun.* **6**, 7638 (2015).
- Adams, T. et al. Long-range crystalline nature of the skyrmion lattice in mnsi. *Phys. Rev. Lett.* **107**, 217206 (2011).
- Woo, S. et al. Observation of room-temperature magnetic skyrmions and their current-driven dynamics in ultrathin metallic ferromagnets. *Nat. Mater.* **15**, 501–506 (2016).
- Wiesendanger, R. Nanoscale magnetic skyrmions in metallic films and multilayers: a new twist for spintronics. *Nat. Rev. Mater.* **1**, 16044 (2016).
- Kiselev, N. S., Bogdanov, A. N., Schäfer, R. & Rößler, U. K. Chiral skyrmions in thin magnetic films: new objects for magnetic storage technologies? *J. Phys. D: Appl. Phys.* **44**, 392001 (2011).
- Yu, X. Z. et al. Near room-temperature formation of a skyrmion crystal in thin-films of the helimagnet fege. *Nat. Mater.* **10**, 106–109 (2011).
- Yu, X. Z. et al. Real-space observation of a two-dimensional skyrmion crystal. *Nature* **465**, 901–904 (2010).
- Heinze, S. et al. Spontaneous atomic-scale magnetic skyrmion lattice in two dimensions. *Nat. Phys.* **7**, 713–718 (2011).
- Skyrme, T. H. R. A unified field theory of mesons and baryons. *Nucl. Phys.* **31**, 556–569 (1962).
- Schulz, T. et al. Emergent electrodynamics of skyrmions in a chiral magnet. *Nat. Phys.* **8**, 301–304 (2012).
- Milde, P. et al. Unwinding of a skyrmion lattice by magnetic monopoles. *Science* **340**, 1076–1080 (2013).
- Schütte, C. & Rosch, A. Dynamics and energetics of emergent magnetic monopoles in chiral magnets. *Phys. Rev. B* **90**, 174432 (2014).
- Neubauer, A. et al. Topological hall effect in the a phase of mnsi. *Phys. Rev. Lett.* **102**, 186602 (2009).
- Jiang, W. et al. Direct observation of the skyrmion hall effect. *Nat. Phys.* **13**, 162–169 (2017).
- Kanazawa, N. et al. Discretized topological hall effect emerging from skyrmions in constricted geometry. *Phys. Rev. B* **91**, 041122 (2015).
- Seki, S., Yu, X. Z., Ishiwata, S. & Tokura, Y. Observation of skyrmions in a multiferroic material. *Science* **336**, 198–201 (2012).
- Jonietz, F. et al. Spin transfer torques in mnsi at ultralow current densities. *Science* **330**, 1648–1651 (2010).
- Zhang, X., Ezawa, M. & Zhou, Y. Magnetic skyrmion logic gates: conversion, duplication and merging of skyrmions. *Sci. Rep.* **5**, 9400 (2015).
- Sampaio, J., Cros, V., Rohart, S., Thiaville, A. & Fert, A. Nucleation, stability and current-induced motion of isolated magnetic skyrmions in nanostructures. *Nat. Nanotechnol.* **8**, 839–844 (2013).
- Tomasello, R. et al. A strategy for the design of skyrmion racetrack memories. *Sci. Rep.* **4**, 6784 (2014).
- van der Laan, G., Zhang, S. L. & Hesjedal, T. Depth profiling of 3d skyrmion lattices in a chiral magnet—a story with a twist. *AIP Adv.* **11**, 015108 (2021).
- Zhang, S. et al. Reciprocal space tomography of 3d skyrmion lattice order in a chiral magnet. *Proc. Natl Acad. Sci. USA* **115**, 6386–6391 (2018).
- Iwasaki, J., Mochizuki, M. & Nagaosa, N. Current-induced skyrmion dynamics in constricted geometries. *Nat. Nanotechnol.* **8**, 742–747 (2013).
- Birch, M. T. et al. Topological defect-mediated skyrmion annihilation in three dimensions. *Commun. Phys.* **4**, 175 (2021).
- Kagawa, F. et al. Current-induced viscoelastic topological unwinding of metastable skyrmion strings. *Nat. Commun.* **8**, 1332 (2017).
- Birch, M. et al. Real-space imaging of confined magnetic skyrmion tubes. *Nat. Commun.* **11**, 1726 (2020).
- Yu, X. et al. Real-space observation of topological defects in extended skyrmion-strings. *Nano Lett.* **20**, 7313–7320 (2020).
- Wolf, D. et al. Unveiling the three-dimensional magnetic texture of skyrmion tubes. *Nat. Nanotechnol.* **17**, 250–255 (2022).
- Koshibae, W. & Nagaosa, N. Dynamics of skyrmion in disordered chiral magnet of thin film form. *Sci. Rep.* **9**, 5111 (2019).
- Du, H. et al. Edge-mediated skyrmion chain and its collective dynamics in a confined geometry. *Nat. Commun.* **6**, 8504 (2015).

33. Meynell, S. A., Wilson, M. N., Fritzsche, H., Bogdanov, A. N. & Monchesky, T. L. Surface twist instabilities and skyrmion states in chiral ferromagnets. *Phys. Rev. B* **90**, 014406 (2014).
34. Streubel, R. et al. Retrieving spin textures on curved magnetic thin films with full-field soft x-ray microscopies. *Nat. Commun.* **6**, 7612 (2015).
35. Blanco-Roldán, C. et al. Nanoscale imaging of buried topological defects with quantitative x-ray magnetic microscopy. *Nat. Commun.* **6**, 8196 (2015).
36. Donnelly, C. et al. Tomographic reconstruction of a three-dimensional magnetization vector field. *N. J. Phys.* **20**, 083009 (2018).
37. Donnelly, C. & Scagnoli, V. Imaging three-dimensional magnetic systems with x-rays. *J. Phys.: Condens. Matter* **32**, 213001 (2020).
38. Seki, S. et al. Direct visualization of the three-dimensional shape of skyrmion strings in a noncentrosymmetric magnet. *Nat. Mater.* **21**, 181–187 (2021).
39. Gilbert, D. A. et al. Precipitating ordered skyrmion lattices from helical spaghetti and granular powders. *Phys. Rev. Mater.* **3**, 014408 (2019).
40. Henderson, M. E. et al. Characterization of a disordered above room temperature skyrmion material $\text{Co}_8\text{Zn}_8\text{Mn}_4$. *Materials* **14**, 4689 (2021).
41. Henderson, M. et al. Skyrmion alignment and pinning effects in the disordered multiphase skyrmion material $\text{Co}_8\text{Zn}_8\text{Mn}_4$. *Phys. Rev. B* **106**, 094435 (2022).
42. Heacock, B. et al. Neutron sub-micrometre tomography from scattering data. *IUCrJ* **5**, 893–900 (2020).
43. Sidky, E. Y. & Pan, X. Image reconstruction in circular cone-beam computed tomography by constrained, total-variation minimization. *Phys. Med. Biol.* **53**, 4777 (2008).
44. Zhang, S. L., van der Laan, G., Wang, W. W., Haghighirad, A. A. & Hesjedal, T. Direct observation of twisted surface skyrmions in bulk crystals. *Phys. Rev. Lett.* **120**, 227202 (2018).
45. Karube, K. et al. Robust metastable skyrmions and their triangular-square lattice structural transition in a high-temperature chiral magnet. *Nat. Mater.* **15**, 1237–1242 (2016).
46. Karube, K. et al. Metastable skyrmion lattices governed by magnetic disorder and anisotropy in β -Mn-type chiral magnets. *Phys. Rev. B* **102**, 064408 (2020).
47. Preißinger, M. et al. Vital role of magnetocrystalline anisotropy in cubic chiral skyrmion hosts. *npj Quantum Mater.* **6**, 2397–4648 (2021).
48. Henderson, M. E. et al. Supplemental videos for: Three-dimensional neutron far-field tomography of a bulk skyrmion lattice. *Zenodo* <https://doi.org/10.5281/zenodo.7115410> (2022).
49. Birch, M. T. et al. Anisotropy-induced depinning in the Zn-substituted skyrmion host Cu_2OSeO_3 . *Phys. Rev. B* **102**, 104424 (2020).
50. Karube, K. et al. Skyrmion formation in a bulk chiral magnet at zero magnetic field and above room temperature. *Phys. Rev. Mater.* **1**, 074405 (2017).
51. McCray, A. R. C. et al. Thermal hysteresis and ordering behavior of magnetic skyrmion lattices. *Nano Lett.* **22**, 7804–7810 (2022).
52. Leonov, A. O. & Inoue, K. Homogeneous and heterogeneous nucleation of skyrmions in thin layers of cubic helimagnets. *Phys. Rev. B* **98**, 054404 (2018).
53. Oike, H. et al. Interplay between topological and thermodynamic stability in a metastable magnetic skyrmion lattice. *Nat. Phys.* **12**, 62–66 (2016).
54. Tokura, Y. & Kanazawa, N. Magnetic skyrmion materials. *Chem. Rev.* **121**, 2857–2897 (2021).
55. Mathur, N. et al. In-plane magnetic field-driven creation and annihilation of magnetic skyrmion strings in nanostructures. *Adv. Funct. Mater.* **31**, 2008521 (2021).
56. Zheng, F. et al. Experimental observation of chiral magnetic bobbles in b20-type FeGe. *Nat. Nanotechnol.* **13**, 451–455 (2018).
57. Sarenac, D. et al. Generation and detection of spin-orbit coupled neutron beams. *Proc. Natl Acad. Sci. USA* **116**, 20328–20332 (2019).
58. Clark, C. W., Barankov, R., Huber, M. G., Cory, D. G. & Pushin, D. A. Controlling neutron orbital angular momentum. *Nature* **525**, 504–506 (2015).
59. Sarenac, D. et al. Experimental realization of neutron helical waves. *Sci. Adv.* **8**, eadd2002 (2022).

Publisher's note Springer Nature remains neutral with regard to jurisdictional claims in published maps and institutional affiliations.

Open Access This article is licensed under a Creative Commons Attribution 4.0 International License, which permits use, sharing, adaptation, distribution and reproduction in any medium or format, as long as you give appropriate credit to the original author(s) and the source, provide a link to the Creative Commons license, and indicate if changes were made. The images or other third party material in this article are included in the article's Creative Commons license, unless indicated otherwise in a credit line to the material. If material is not included in the article's Creative Commons license and your intended use is not permitted by statutory regulation or exceeds the permitted use, you will need to obtain permission directly from the copyright holder. To view a copy of this license, visit <http://creativecommons.org/licenses/by/4.0/>.

© The Author(s) 2023

Methods

The $\text{Co}_5\text{Zn}_8\text{Mn}_4$ material was grown via a modified Bridgman technique in a rapid high-temperature furnace at McMaster University, before being cut into a cube of dimensions $3.4 \text{ mm} \times 3.3 \text{ mm} \times 3.0 \text{ mm}$ and oriented such that the (100) direction was coming out of the major face. Details of the sample, as well as single-projection SANS and susceptibility measurements, are available elsewhere⁴⁰.

Multiprojection, unpolarized SANS was performed at the NG7-30m beamline at the National Institute for Standards and Technology (NIST) for a 15 m beam configuration at a wavelength of 6 \AA . The sample was field cooled from 420 K in a field of 250 G to 310 K. Upon entering the thermal equilibrium triangular lattice skyrmion phase a uniform ring manifested in SANS, indicative of a jammed chiral state composed of misoriented skyrmion, labyrinth and helical domains⁴¹. The skyrmion sample was rotated symmetrically in the magnetic field 10 times over a $\pm 60^\circ$ angular range to achieve the ordered six-fold pattern shown in Fig. 1. From here, multiprojection SANS data were collected for a static skyrmion configuration, rotating the sample and field together on the same rotation stage about the vertical axis specified in Fig. 1 to ensure the magnetic field orientation remained fixed—with the field direction parallel to the surface normal of the sample. These tomographic rotations were performed for 30 angles from -2.9° to 2.9° . Incorporating additional tomography axes may enhance the data, particularly in the case of sample tilting for skyrmion states with very short longitudinal correlation lengths; however, this is left for our future studies.

Digital phantoms were made by seeding a log-likelihood gain relaxation using Ubermag⁶⁰ with a high-energy lattice made to have a fixed correlation volume. The log-likelihood gain relaxation was stopped after ten iterations to retain a reasonable density of defects. The system used the free-energy functional

$$E[\mathbf{m}] = -A\mathbf{m} \cdot \nabla^2 \mathbf{m} + D\mathbf{m} \cdot (\nabla \times \mathbf{m}) - \mu_0 M_s \mathbf{H} \cdot \mathbf{m} \quad (1)$$

with exchange stiffness $A = 10 \text{ pJ m}^{-1}$, Dzyaloshinskii–Moriya constant $D = 3.93 \times 10^{-3} \text{ J m}^{-1}$, saturation magnetization $M_s = 1 \times 10^6 \text{ A m}^{-1}$ and external field values of $\mathbf{H} = 0.2080 \text{ T}$, 0.2780 T and 0.3475 T for phantoms A, B and C, respectively.

The seed was generated by alternating between Fourier-space and real-space constraints. The magnitude of the sample magnetization in Fourier space is set by desired correlation volume, the real-space magnitude of the sample magnetization was constrained to unity everywhere and the transverse magnetization was set to be in the direction of the curl of the longitudinal magnetization.

SANS patterns were simulated by applying a forward operator to a randomly selected and randomly translated phantom of 20 phantoms made with differing random initialization. The resulting SANS images produced by repeating this process at least 100 times were averaged to simulate an incoherent neutron source and create the resulting simulated multiprojection SANS data.

The voxel size of the MSFR is determined by the Fourier-space span of the SANS images $dx = 2\pi/Q_{\text{tot}} = 2\pi/(dQN)$. In this experiment $dx = 14.3 \text{ nm}$, as determined by the resolution $dQ = 3.4 \mu\text{m}^{-1}$ and size $N \times N = 128 \times 128$ of the SANS images. The height of the MSFR was set to 256 voxels, for a total volume of $1.8 \mu\text{m} \times 1.8 \mu\text{m} \times 3.7 \mu\text{m} = 12.3 \mu\text{m}^3$.

To compute the reconstructions, the cost function was minimized using a conjugate gradient method. The $\mathbf{m}^2 = 1$ constraint was enforced by defining search directions in terms of the angular fields $\theta = \arcsin(m_z)$ and $\phi = \arctan(m_y, m_x)$. Ten iterations were run with equal weights for all residuals, which can aid in convergence when measurement uncertainties are dominated by counting statistics and there are regions of low count rates. Following the 10 iterations, 100 iterations were run with the weights given the measurement uncertainties provided by the SANS reduction software⁶¹. A maximum weight was introduced for the low count rate regions to aid in convergence. The resulting average magnetization was found to depend on the weight given to the Zeeman

term h , so reconstructions over a range of h and starting average magnetization (m_z) were performed (Table 1), with the preferred MSFR being the one that most closely matched the phantom or experimental average magnetization.

Details on the forward propagator, gradient and defect density calculations are provided in the Supplementary Information.

Data availability

All experimental and reconstructed data used in this study can be found in an online repository at <https://doi.org/10.5281/zenodo.6828467> (ref. 48). Further materials are available from the corresponding author on reasonable request.

Code availability

The code for the reconstruction algorithm used here is available at <https://doi.org/10.5281/zenodo.8192883> (ref. 62).

References

- Beg, M., Lang, M. & Fangohr, H. Ubermag: Towards more effective micromagnetic workflows. *IEEE Trans. Magn.* **58**, 7300205 (2022).
- Kline, S. R. Reduction and analysis of sans and usans data using igor pro. *J. Appl. Crystallogr.* **39**, 895–900 (2006).
- Henderson, M. E. melissa-e-henderson/Tomo-SANS: Tomo-SANS v1, Zenodo, v1.0, <https://doi.org/10.5281/zenodo.8192883> (2023).

Acknowledgements

We thank D. Gilbert for suggesting that skyrmion systems would be an interesting subject to study with SANS tomography. This work was supported by the Canadian Excellence Research Chairs programme, the Natural Sciences and Engineering Council of Canada Discovery programme, the Canada First Research Excellence Fund and the NIST, and the US Department of Energy, Office of Nuclear Physics, under Interagency Agreement no. 89243019SSCO00025. Access to SANS and the Center for High Resolution Neutron Scattering (CHRNS) was provided by CHRNS, a partnership between NIST and the National Science Foundation under Agreement No. DMR-1508249.

Author contributions

M.E.H., B.H., D.S. and D.A.P. conceived and performed the project. D.A.P., M.B., B.H., M.E.H., M.B., J.K., M.G.H. and K.Z. performed the SANS experiment. M.E.H., M.P. and G.M.L. performed preliminary sample characterization and magnetic susceptibility measurements. B.H., M.E.H. and O.N.L. developed and tested the reconstruction algorithm and phantom datasets. M.E.H. and B.H. wrote the paper. All authors contributed to data analysis and paper revisions.

Competing interests

The authors declare no competing interests.

Additional information

Supplementary information The online version contains supplementary material available at <https://doi.org/10.1038/s41567-023-02175-4>.

Correspondence and requests for materials should be addressed to M. E. Henderson or D. A. Pushin.

Peer review information *Nature Physics* thanks Nicolas Martin, Markus Strobl and the other, anonymous, reviewer(s) for their contribution to the peer review of this work.

Reprints and permissions information is available at www.nature.com/reprints.